

Article

Graphene-Based TiO₂ Cement Composites to Enhance the Antibacterial Effect of Self-Disinfecting Surfaces

Abdul Halim Hamdany^{1,2,*} , Yuanzhao Ding³  and Shunzhi Qian^{2,*}

¹ Department of Civil and Environmental Engineering, Faculty of Engineering, University of Indonesia, Depok 16424, Indonesia

² School of Civil and Environmental Engineering, Nanyang Technological University, 50 Nanyang Avenue, Singapore 639798, Singapore

³ School of Geography and the Environment, Oxford University, S Parks Rd, Oxford OX1 3QY, UK; armstrongding@163.com

* Correspondence: abdul.halim04@office.ui.ac.id (A.H.H.); szqian@ntu.edu.sg (S.Q.)

Abstract: This paper studies the photocatalytic performance of graphene-based titanium dioxide (TiO₂) on cementitious composites for the decomposition of *Escherichia coli* (*E. coli*) under visible light. Graphene-based TiO₂ was first synthesized through a hydrothermal process. The composites were then evaluated in terms of adsorption capability and degradation of methylene blue dyes. The adsorption test shows a remarkable increase in the amount of dye adsorbed into the composite surface. GO-P25 could adsorb around 60% of the initial dye, while less than 10% of the initial dye was adsorbed by pristine TiO₂-P25. The synthesized graphene-based TiO₂ significantly enhanced the dye degradation activity (94%) compared to pristine P25 (36%) and Krono (52%), even with the longer irradiation time for P25 and Krono. This led to an increase in reaction rate that was almost 20 times that of P25. Considering the good adsorption capabilities and high photodegradation of dye under visible light for GO-P25, cement-based surfaces containing GO-P25 are expected to be improved for the decomposition of *Escherichia coli* (*E. coli*) under visible light. Graphene-based TiO₂ on a cement-based surface showed high antibacterial activity with a 77% reduction in number of bacteria compared to a cement-based surface containing pristine TiO₂. This study confirms the effectiveness of the composites for disinfection of *E. coli* under visible light.

Keywords: self-sterilization surface; cementitious composites; titanium dioxide; graphene oxide; *Escherichia coli* inactivation



Citation: Hamdany, A.H.; Ding, Y.; Qian, S. Graphene-Based TiO₂ Cement Composites to Enhance the Antibacterial Effect of Self-Disinfecting Surfaces. *Catalysts* **2023**, *13*, 1313. <https://doi.org/10.3390/catal13091313>

Academic Editors: Zhengxian Yang, Lu Yang and Manuel Filipe P. C. M. Costa

Received: 24 July 2023

Revised: 16 September 2023

Accepted: 18 September 2023

Published: 21 September 2023



Copyright: © 2023 by the authors. Licensee MDPI, Basel, Switzerland. This article is an open access article distributed under the terms and conditions of the Creative Commons Attribution (CC BY) license (<https://creativecommons.org/licenses/by/4.0/>).

1. Introduction

Since Fujishima and Honda [1] introduced the scientific concept of photocatalysis, an enormous amount of research has been carried out to understand the fundamental mechanism and further improve the efficiency of various photocatalysts. In recent years, titanium dioxide (TiO₂) has been proven to be the most suitable photocatalyst for environmental control due to its capability to completely destroy a large variety of organic pollutants [2,3]. Titanium dioxide particles are abundant, economical, relatively non-toxic, and highly photoactive, yet chemically stable and resistant to photocorrosion [4–6]. However, the wide bandgap of pristine TiO₂ hinders its full potential for many applications [7,8]. The bandgap of TiO₂ lies in the UV region, which is only 3–5% of sunlight energy. Therefore, one of the main challenges in improving the performance of TiO₂ photocatalysts is to extend their optical response from the UV to the visible region.

The optical response of TiO₂ can be improved by substituting the metal (titanium) or the non-metal (oxygen) component, which is called the doping technique [9,10]. Alternatively, it can be achieved by surface modifications or photosensitization, in which the charge injection process is induced by the match of energy difference between the oxidation potential of the excited sensitizer and TiO₂ conduction band [11–14]. Previous

studies have reported that the improvement of TiO₂ activity under visible light could be achieved by surface modifications with carbonaceous materials such as graphene oxide (GO) [15–22]. This composite can be synthesized via different methods, for example, the sol–gel method, hydrothermal/solvothermal technique, or even a simple mixing process. The sol–gel method typically starts with solutions consisting of metal compounds (sol) as a precursor [23]. Further reaction integrates the network between particles, solidifying the sol into a gel. Sol–gel routes afford excellent control of nanosized particles, shape distribution, and crystallinity. However, it has a number of disadvantages, such as being substrate dependent (its typical precursor is metal alkoxides which are high-cost materials) and time-consuming due to the slow process of gel formation [24]. The hydrothermal technique involves single or heterogeneous phase reactions under controlled temperature and pressure to crystallize a substance from an aqueous solution [19,25,26]. It allows shorter processing time and lower energy consumption, since the high calcination temperature, mixing, and milling can be minimized. The need for expensive autoclaves is one of the main disadvantages of these methods.

Early works of TiO₂ application focused on water remediation, in which the separation process became the main drawback for widespread application [3,27]. The use of TiO₂ heterogeneous photocatalysis on cementitious composites highly elevates its utilization from a practical point of view. The introduction of a suitable amount of TiO₂ into cementitious composites could result in the surface of composites becoming photo-catalytically active [28,29]. Cementitious composite in building façades or paving blocks in pedestrian walkways could be utilized as catalyst-supporting media to provide a huge amount of surface area available for photocatalytic processes during the day when exposed to the sunlight. The shift of TiO₂ optical response from the UV to the visible light region could greatly improve the efficiency of the photocatalysis process. Cementitious composites could be tailored to have beneficial unique features, such as self-cleaning surfaces, air-purification functions, and antibacterial effects [30–37].

Compared with air purification and self-cleaning applications [30,32,38,39], little research has been carried out to investigate the antibacterial effect of photocatalytic cementitious materials. This work will evaluate the application of a GO-TiO₂ composite in a cement-based surface for an antibacterial test. It starts with the preparation of graphene-based TiO₂ nanocomposites via a one-step hydrothermal process. An adsorption test and methylene blue degradation test were conducted to evaluate the photocatalytic performance under visible light illumination. An antibacterial surface test was also conducted to examine the cement-based surface containing GO-TiO₂ nanocomposite for decomposition of *Escherichia coli* (*E. coli*).

2. Results

2.1. TiO₂ Characterization

Two commercial TiO₂ samples and a synthesized graphene-based TiO₂ were evaluated in this characterization test. Surface morphologies and the particle size of nanoparticles used in this work were examined using field emission scanning electron microscopy (FESEM). Figure 1 shows the FESEM image for P25, Krono, and GO-P25. The primary particle size of P25, Krono, and GO-P25 was approximately 20–40 nm in diameter. However, the primary particles of the Krono samples showed a strong tendency to agglomerate to form larger secondary particles with a diameter of more than 500 nm, contributing to the porous structure. On the other hand, no significant difference was observed between the morphology of P25 and the morphology of synthesized GO-P25. This result was consistent with past studies [33,40,41], indicating the low ratio of GO did not create a significant change to the appearance of pristine TiO₂ nanoparticles.

The crystal structure of TiO₂ nanomaterials was analysed using an X-ray diffractometer technique. Figure 2 presents the XRD patterns of P25, GO-P25, and Krono. The P25 sample consists of anatase and rutile phase while the Krono sample only consists of the anatase phase. Identical crystal structures were observed between pristine P25 and graphene-

modified P25. In line with the morphology test, a low amount of GO resulted in the absence of diffraction peaks for carbon species. This finding was supported by a previous study indicating that modification of TiO₂ with a graphene layer did not change the crystal structure of TiO₂ [20,21].

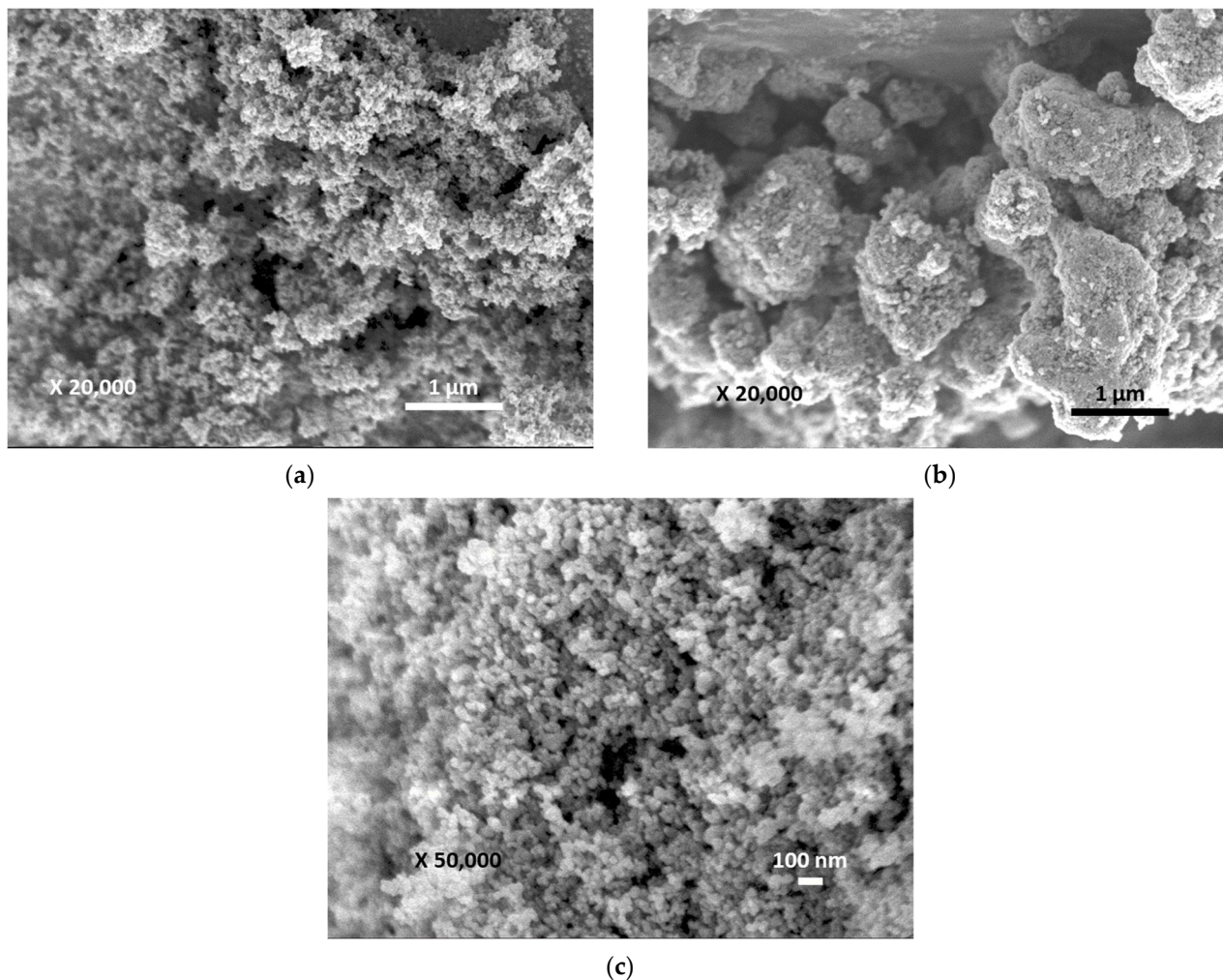


Figure 1. FESEM images of (a) P25, (b) Krono, and (c) GO-P25.

Ultraviolet–visible diffuse reflectance Spectrophotometer (UV-vis DRS) was utilized to evaluate the optical properties of TiO₂ photocatalysts used in this study. Figure 3 presents the optical absorption spectrum of P25, Krono, and GO-P25. Their corresponding $(\alpha hv)^{1/2}$ versus photon energy are presented as well. Figure 3a showed that P25 and Krono had no absorption in the visible light range. Using the Kubelka–Munk model, the bandgap energy could be determined from the absorption spectra and plotted using Tauc’s relation:

$$\alpha hv = \text{const}(hv - E_g)^2$$

where α is the absorption coefficient; hv is the energy of the incident photon; E_g is the optical bandgap of materials. Tauc’s plot displays the quantity of photon energy (hv) on the x-coordinate and the quantity of $(\alpha hv)^{1/2}$ on the y-coordinate. As shown in Figure 3, the results indicated that the GO-P25 composite showed strong absorption in the visible light range and a narrower bandgap compared to P25 and Krono. The estimated bandgap values for P25, Krono, and GO-P25 are 3.21, 3.24, and 3.09, respectively, as presented in Figure 3b.

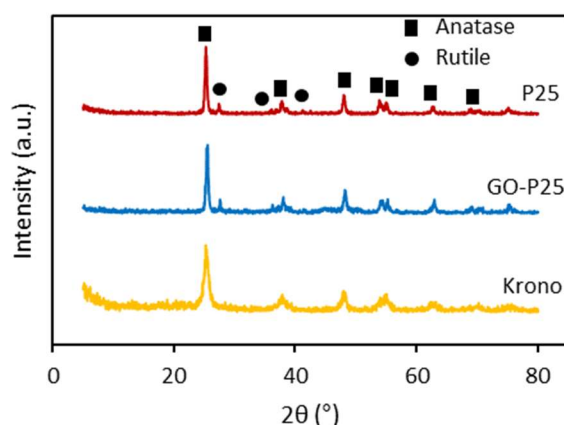


Figure 2. XRD result of 25, Krono, and GO-P25.

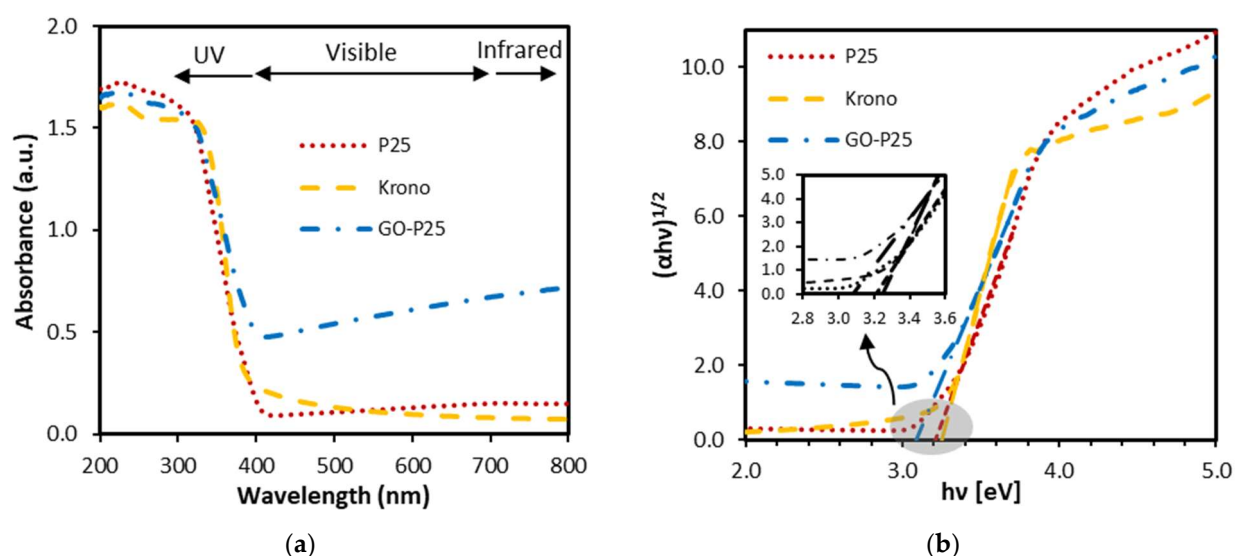


Figure 3. (a) Optical absorption of P25, Krono, and GO-P25 and (b) bandgap determination of P25, Krono, and GO-P25.

Nitrogen adsorption technique was conducted to determine the specific surface area and pore structure of the nanoparticles. Figure 4 shows the nitrogen adsorption/desorption isotherm according to the Brunauer–Emmett–Teller (BET) method and pore size distribution according to the Barrett–Joyner–Halenda (BJH) method. According to the International Union of Pure and Applied Chemistry (IUPAC) classification, the N_2 adsorption/desorption isotherm of Krono showed the characteristic of mesoporous materials, a typical type IV isotherm. The result was in line with the FE-SEM image showing the porous structure of Krono samples. The BET specific surface area (SSA) and pore volume of Krono were $252.1 \text{ m}^2/\text{g}$ and $0.09 \text{ cm}^3/\text{g}$, respectively, while the SSA and pore volume of P25 were $46.9 \text{ m}^2/\text{g}$ and $0.01 \text{ cm}^3/\text{g}$, respectively. The observed high SSA and high pore volume of Krono could facilitate the diffusion of contaminants or other microbial organisms through the pores to access the active site. The BJH pore size distribution study indicates that Krono had a very small pore diameter around 2–3 nm.

2.2. Adsorption Capability

The adsorption capability is one of the important factors that influences the overall photocatalytic efficiencies [5,10,20,21]. Therefore, an investigation of adsorption capability was carried out before starting the irradiation. The purpose of the adsorption test was to study the effect of the combination of GO and TiO_2 on the adsorption of contaminants. Methylene blue dye was used in this test as the target contaminant. Methylene blue was a

popular cationic dye that was commonly used as a synthetic dye in textile industries. In a typical procedure, the photocatalyst powder was dispersed in a methylene blue solution. The solution was then kept in the dark with incessant stirring for 30 min to reach the adsorption equilibrium. The UV absorption spectra of methylene blue after the adsorption test are shown in Figure 5. The peak intensity at 664 nm shows the concentration of dye. The decrease in such a peak indicated the amount of dye adsorbed by composite materials.

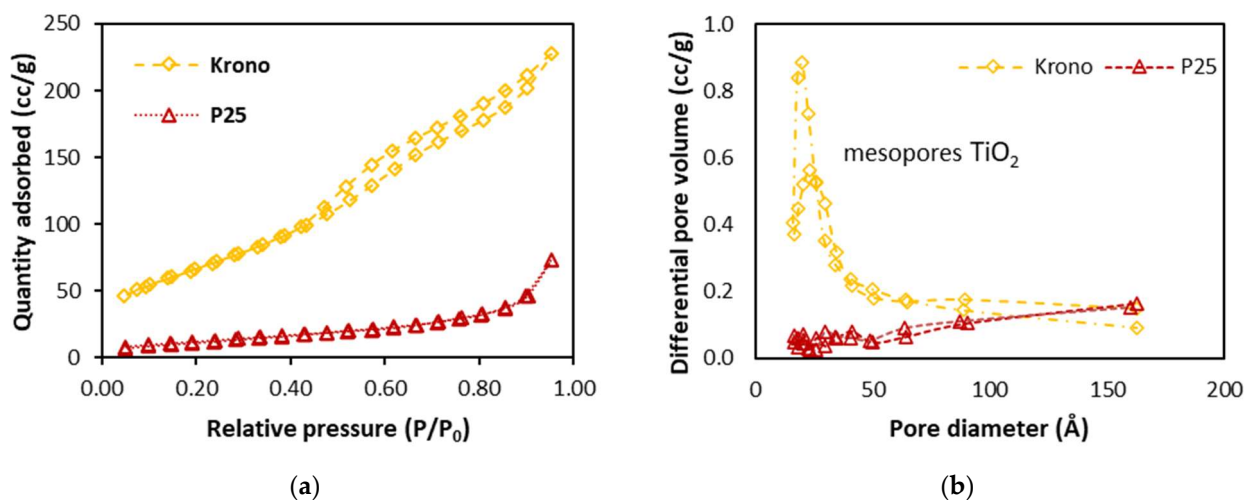


Figure 4. (a) BET nitrogen adsorption–desorption isotherm and (b) BJH pore size distribution.

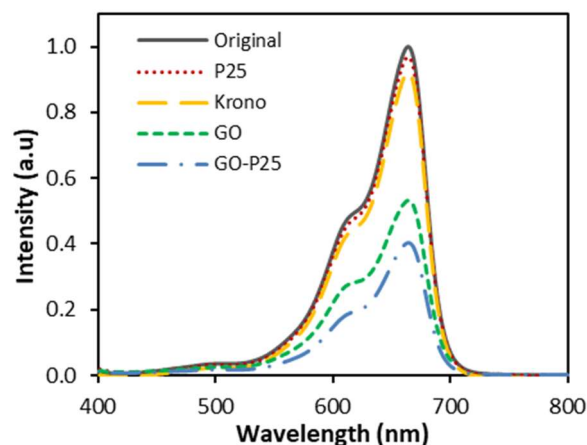


Figure 5. UV absorption spectra of methylene blue after adsorption test.

As shown in Figure 5, approximately 60% of the initial dye was adsorbed by graphene-based titanium dioxide while only less than 10% of the initial dye was adsorbed by commercially available TiO₂, P25, and Krono. The enhancement of adsorption capability was generally attributed to the increase in specific surface area [42,43]. However, higher SSA from Krono ($SSA_{Krono} = 252.1 \text{ m}^2/\text{g}$) was not followed by a significant increase in its adsorption capability. One of the main reasons was the contaminant (MB in this case) had a bigger size (MB size $> 71 \mu\text{m}$) compared to the pore diameter of mesoporous Krono samples (pore diameter of Krono = 2 nm), which resulted in low adsorption capability.

On the other hand, according to BET result, the specific surface areas for GO-P25 increased only around 17% ($SA_{P25} = 46.89 \text{ m}^2/\text{g}$ and $SSA_{GO-P25} = 54.92 \text{ m}^2/\text{g}$) but adsorption capability greatly increased from 10% to 60%. This finding was consistent with earlier studies, which suggested that the reason for the enhanced adsorption capability was not only due to the increase in specific surface area but also due to the non-covalent interactions (π - π interaction) between graphene layer and methylene blue dye [21,35]. The electrostatic interaction between methylene blue dye (+11.3 mV, cationic dye) and the surface

of graphene oxide (-7.87 mV, negatively charged) had a significant effect on increasing adsorption capacity.

2.3. Photodegradation of Dye

Figure 6 presents the photodegradation of methylene blue over P25, Krono, and GO-P25 under visible light irradiation. It showed that the combination of GO and TiO_2 significantly enhanced the photodegradation of the dye compared to pristine P25 and Krono (Figure 6). For the GO-P25 composite materials, 94% of the initial dye was degraded after 1 h irradiation; on the contrary, only 36% of the initial dye was decomposed by P25 even with a longer irradiation time of 4 h. Photocatalytic activity of Krono in visible light was better than that of P25 where 51% of the initial dye was degraded after 4 h irradiation. In the absence of a photocatalyst, approximately only 3% of the methylene blue was decomposed due to direct photolysis of the dye. As a control, the degradation performance of GO was also observed to exclude the impact of GO during the photodegradation process. In the presence of GO, the concentration of dye remained unchanged after achieving adsorption equilibrium (Figure 6), suggesting that the GO alone did not show photocatalytic activity.

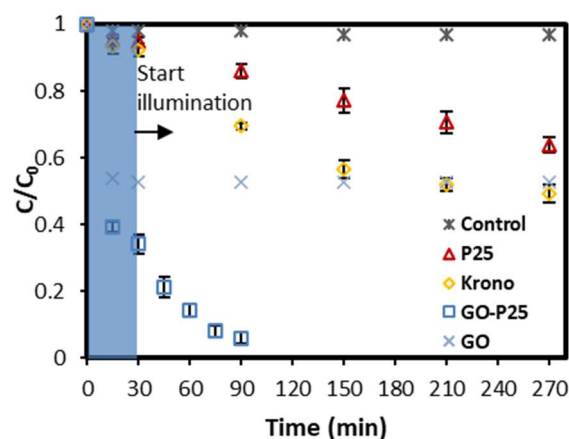


Figure 6. Photodegradation of methylene blue over P25, Krono, and GO-P25 under visible light irradiation.

The modified Langmuir–Hinshelwood (L-W) equation was utilized to evaluate the reaction rate of photocatalytic activity.

$$\frac{dC}{dt} = \frac{k_r K_e C}{1 + K_e C}$$

expressed in integral form gave:

$$t = \frac{1}{K_e k_r} \ln \frac{C}{C_0} + \frac{1}{k_r} (C_0 - C)$$

as the condition of the experiment was carried out under low concentration of the dye ($\ll 10^{-3}$), the equation can be expressed as:

$$\ln \frac{C}{C_0} = k_r K_e t = k' t$$

where C and C_0 were the dye concentration at time t and initial concentration ($t = 0$), k_r was the apparent reaction rate constant; K_e was the apparent equilibrium constant for the dye to adsorb onto the surface of the photocatalyst; k' was the overall rate constant.

Figure 7 shows $\ln(C/C_0)$ has a linear relationship with irradiation time for different photocatalysts (P25, Krono, and GO-P25). Hence, the photocatalytic reaction rate was described by the first-order kinetic model. The slope of the line in Figure 7 could represent the reaction rates for photodegradation of methylene blue with $k'_{GO-P25} \gg k'_{Krono} > k'_{P25}$.

It clearly displayed a great improvement in the degradation rate for GO-P25 compared to P25 and Krono. GO-P25 showed the best degradation of methylene blue, giving the highest reaction rate of 0.0299. This gave a reaction rate that is almost 20 times that of P25.

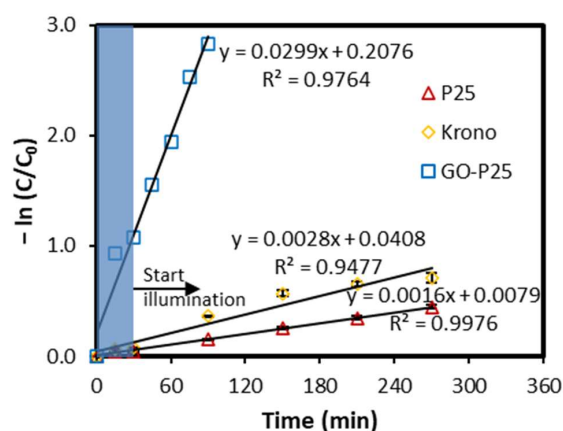


Figure 7. Degradation rate for pristine TiO_2 and GO- TiO_2 composite.

2.4. *Escherichia coli* Disinfection

Considering the good adsorption capabilities and high activity on MB degradation under visible light for GO-P25 nanocomposite materials, the antibacterial performances of such composite materials were expected to be improved than that of pristine TiO_2 . As presented in Figure 8, the bacteria were significantly killed after 60 min incubation with nanocomposite materials. The total number of bacteria was reduced by around 77% after 60 min incubation with GO-P25. However, the total number of bacteria was only reduced by around 20% for the control group (no TiO_2 addition). As a result, the GO-P25 had the most significant effect in the antibacterial test.

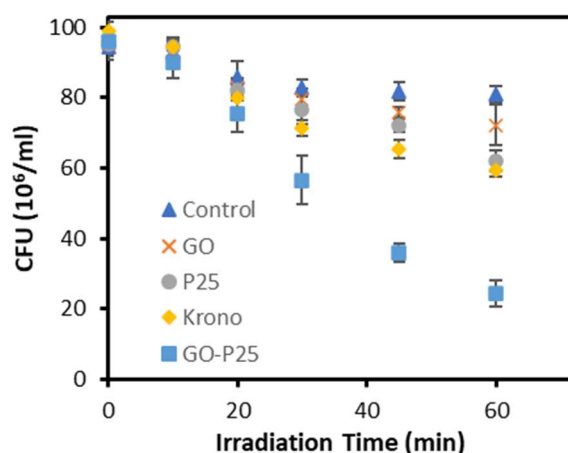


Figure 8. Colony Forming Unit (CFU) test during 60 min incubation with different TiO_2 materials.

The antibacterial effect of GO-P25 nanocomposite materials was observed in earlier studies [33,44,45]. The previous research successfully investigated the antibacterial activity of TiO_2 cementitious composites under visible light using the drop plate method [33], while in this work, the growth pattern and the presence of concomitant bacteria were examined using the Petri dish plate method to quantify the antibacterial effect of cementitious surfaces. The method was employed as an alternative method [46–48] due to its ability to provide a comparative analysis.

The bacteria growth can be visually seen by observing the center part of the agar dish, which is in contact with the cement surface, as shown in Figure 9. The cement sample with 5% GO- TiO_2 loading had the best antibacterial activity compared to the cement sample without TiO_2 and/or with 5% TiO_2 -P25.

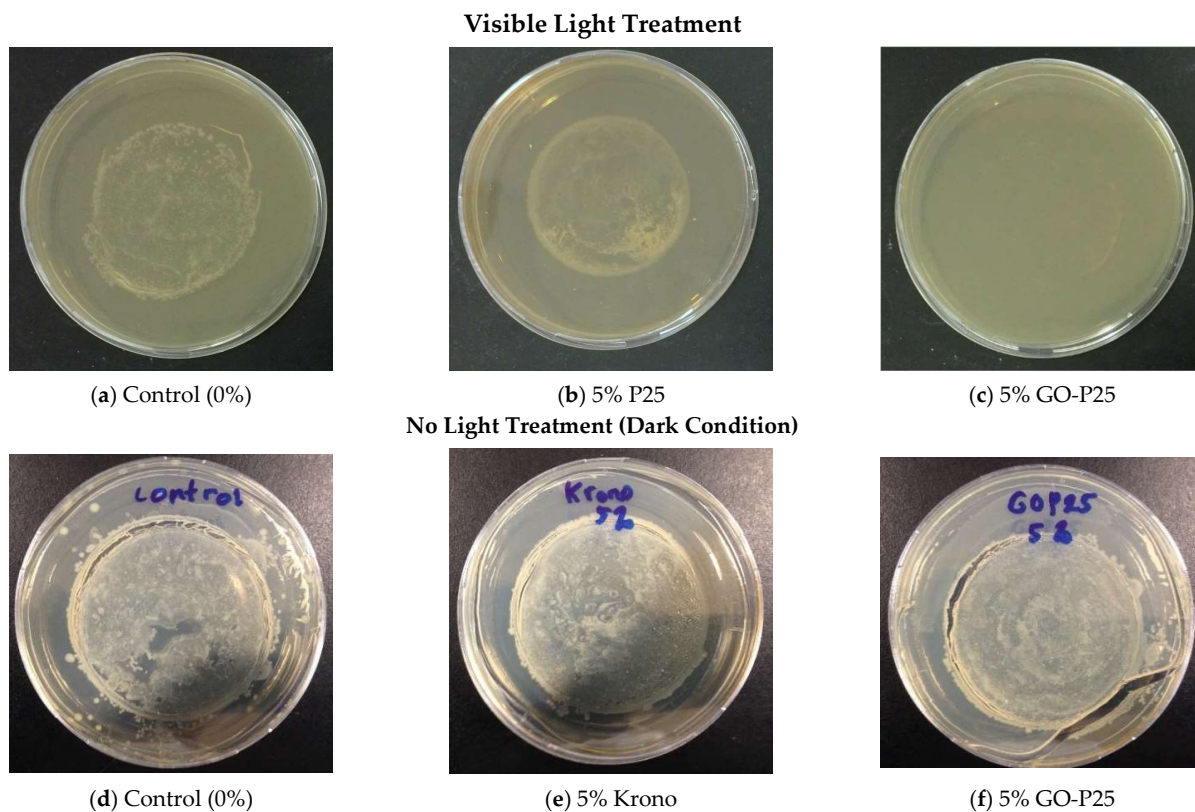


Figure 9. The viability of *E. coli* after 24 h incubation.

Field emission scanning electron microscopy (FESEM) and fluorescence spectroscopy were carried out to investigate whether the *E. coli* cells were really decomposed during photocatalytic treatment. Figure 10 shows the FESEM image and fluorescence image of bacteria decomposition under visible light irradiation with the presence of GO-TiO₂ photocatalyst. It was found that the decomposition of bacterial cells can be achieved in a relatively short time (1 h visible light irradiation).

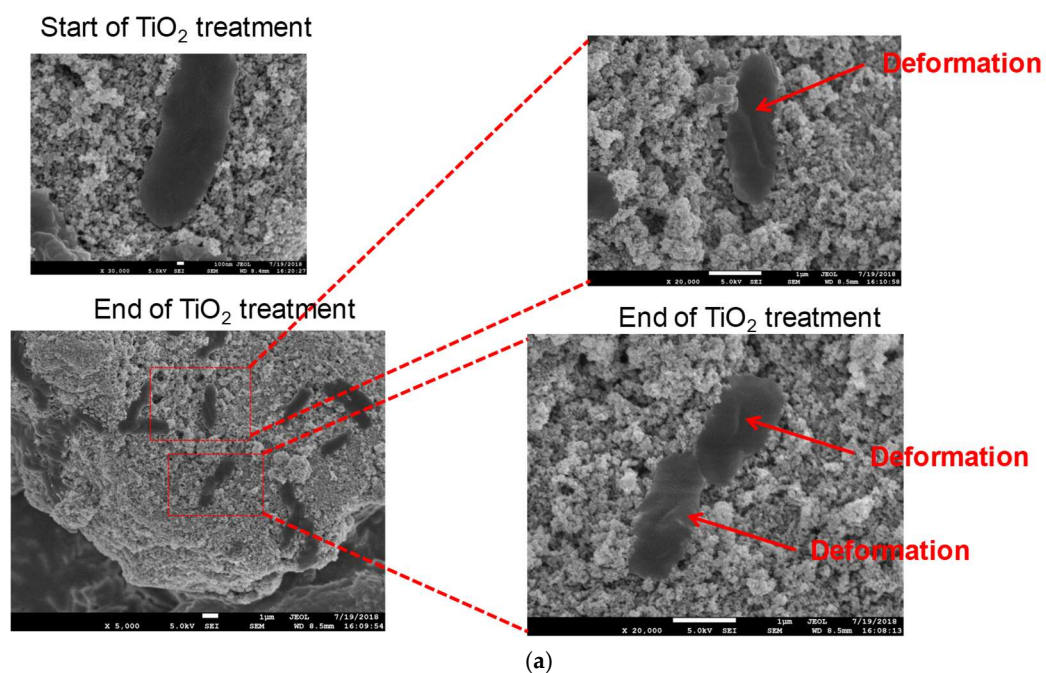


Figure 10. Cont.

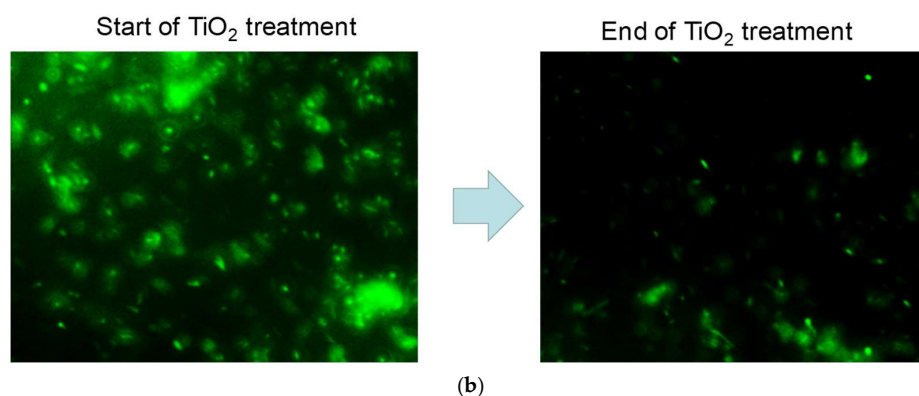


Figure 10. (a) FESEM image and (b) fluorescence image of the decomposition of *E. coli* under visible irradiation on GO-TiO₂ photocatalyst.

3. Discussion

The superior performance of graphene-based TiO₂ composite could be linked to the following reasons. The first reason might be due to the high adsorption capability of the graphene layer in graphene-based TiO₂ composite. The graphene layer could act as photosensitizers by absorbing photon energy under visible light illumination [15,17]. A previous study shows that modification of pristine TiO₂ with graphene could generate the transition band in the middle of the conduction band state of TiO₂, as shown in Figure 11. Under light illumination, an electron in the excited state of the graphene layer could be directly transferred to the conduction band of TiO₂ [17]. Clearly, it produces well-separated hole pairs by creating efficient hole accumulation in the valence band of the graphene layer. The process could significantly reduce charge recombination and become one of the reasons for the enhancement of photovoltaic properties. Subsequently, the electron could be transferred to oxygen adsorbed on the semiconductor surface producing superoxide anion (O₂[−]) which could facilitate the degradation of organic components, as shown in Figure 11. The photodegradation process breaks the adsorption equilibrium, and more dye transfers from the solution to the interface [20,21]. The process is iterated until all the dye is fully decomposed into CO₂, H₂O, and mineral acids. The synergetic effect between adsorption strength and photodegradation may be a key factor in the photocatalytic performance of graphene-based TiO₂ nanocomposite materials.

In an antibacterial process, under visible light irradiation, the injected electron from the excited state graphene layer to the TiO₂ conduction band can induce the reduction of molecular oxygen (O₂) to form the superoxide anion (O₂[−]) [17], as illustrated in Figure 11. It is suggested that superoxide anion could damage iron–sulphur proteins such as aconitase [49,50]. Aconitase is an enzyme that catalyses the interconversion of citrate and isocitrate, which is a series of chemical reactions in the Citric Acid Cycle, that is crucial to aerobic cellular respiration.

Antibacterial GO-P25 nanocomposite materials are highly important because they might have good potential in the application of future hospital construction materials. There are many Hospital-acquired Infection (HAI) cases all over the world. The pathogenic bacteria coming from infected patients may attach to the surfaces of cementitious materials and transfer to another healthy person afterward, which leads to the HAI [51] case. As a result, construction materials with antibacterial effects are strongly needed and may have great potential in future hospital construction.

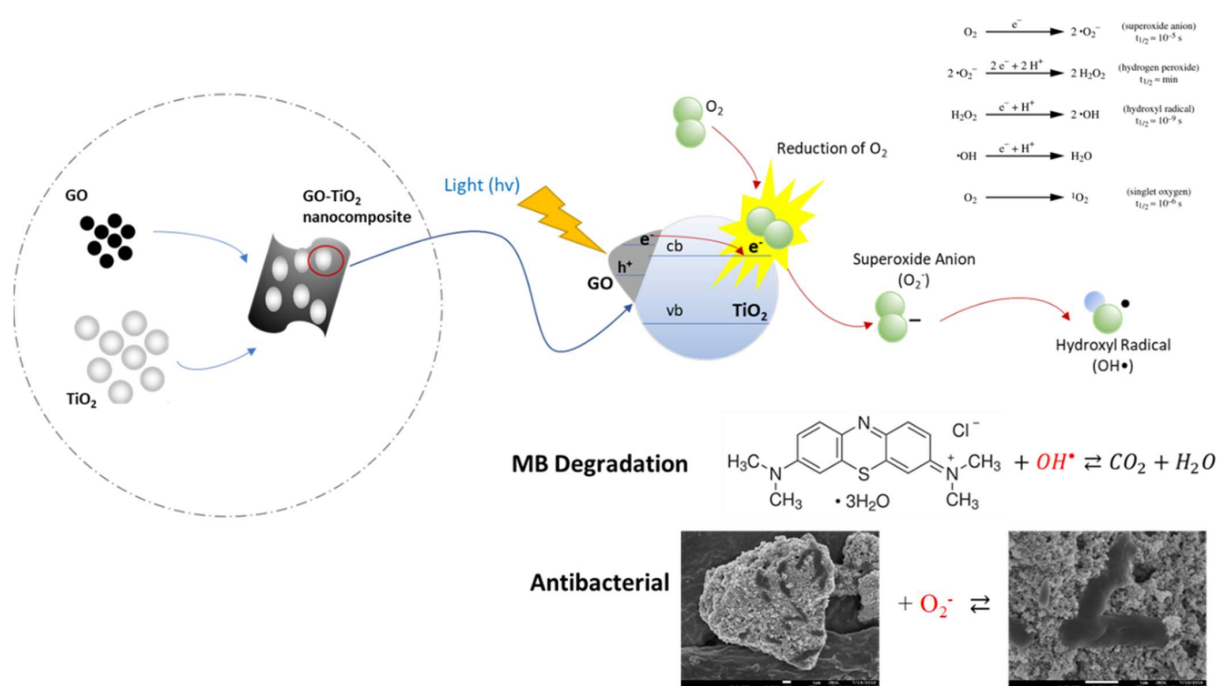


Figure 11. Photocatalytic mechanisms of dye degradation and antibacterial effect under visible light on GO-TiO₂ nanocomposites.

4. Materials and Methods

4.1. Materials

The cementitious material used in this study was white cement from Aalborg Portland, Perak, Malaysia. Aeroxide TiO₂ P25 (Evonik, Essen, Germany) was used as a titanium dioxide catalyst and a precursor for graphene-based titanium dioxide composites. KRONOClean 7000 (KRONOS, Dallas, TX, USA) was used as a control photocatalyst. It was used as a control to compare the performance of the newly synthesised visible light-activated photocatalyst. Graphene oxide with more than 99% purity and research-grade quality was commercially obtained from HENGQIU Technologies, Suzhou, China. It was a small-scale single-layer graphene oxide prepared by the improved hummers method. Methylene blue was used for the photodegradation of dye, and it is obtained commercially from Sigma-Aldrich, Singapore. Bacteria *E. coli* K-12 obtained from the bacterial library in the environment laboratory of Nanyang Technological University was used for an antibacterial test.

4.2. Synthesis of GO-TiO₂ Nanocomposite

Graphene-TiO₂ nanocomposite was prepared through a one-step hydrothermal process using the selected commercial TiO₂ and GO, based on the work of Hamdany, Ding [33], and Zhang, Lv [21] with modifications. The GO loading was kept constant at 3% weight of TiO₂ as an optimum content [42]. Briefly, 242.5 mg of TiO₂ powder was dispersed in 35 mL of distilled water. The TiO₂ solution was then stirred continuously for 30 min at room temperature (≈ 23 – 25 °C) using a magnetic stirrer at 160 rpm. In the meantime, 7.5 mg of graphene oxide was dissolved in 15 mL of distilled water. The GO solution was sonicated at room temperature (≈ 23 – 25 °C) for 30 min using a high-intensity ultrasonic probe. Subsequently, the obtained GO solution was added to the TiO₂ solution under magnetic stirring for another 30 min. The mixture was then stirred at 150° C until all water completely evaporated. Lastly, the obtained solid deposit was then oven-dried for 24 h at 60° C. The final product is referred to as GO-TiO₂.

4.3. Characterization

Field emission scanning electron microscopy (FE-SEM, JSM-7600F, JEOL, Tokyo, Japan) was used to observe the surface morphology of the TiO₂ nanomaterials. The crystallinity of

different types of titanium dioxide materials used in this study was investigated using an X-ray diffractometer (XRD, D8 Advanced, Bruker, Billerica, MA, USA) with monochromatized Cu-K α radiation. The optical properties of the catalysts were investigated using diffuse reflectance spectroscopy (DRS, Cary 5000, Agilent, Santa Clara, CA, USA). The specific surface area of the catalysts was measured by Brunauer–Emmett–Teller (BET) nitrogen adsorption–desorption. The surface charge of TiO₂ materials was assessed by measuring their electro-kinetic potential (zeta potential) via a zeta potential analyser (Zetasizer, Nano ZS, Malvern Panalytical, Malvern, UK). FE-SEM and fluorescence spectroscopy were conducted to examine the decomposition of *E. coli* cells during photocatalytic treatment.

4.4. Cement Sample Preparation

The mix proportions used to prepare the sample are listed in Table 1. Three types of TiO₂ materials were intermixed into cementitious materials with 5% loading. The mixture without any TiO₂ was prepared as control specimens. For sample preparation, cementitious material and TiO₂ were manually mixed as dry powders for 5 min until evenly distributed. Distilled water was then added and manually mixed for another 10 min. The mortar specimens were cast in 60 mm diameter and 15 mm thickness moulds. Three cement discs were prepared for each set. The prepared samples were cured for 28 days at room conditions before tests.

Table 1. Mix proportion (on weight basis of cement).

Mix No	TiO ₂ Type	TiO ₂ Loading	Water Content
1	-	-	
2	P25	5%	0.5
3	Krono	5%	
4	GO-P25	3%	

4.5. Photocatalytic Degradation of Methylene Blue under Visible Light

The degradation of methylene blue was observed based on the absorption spectroscopic technique. In a typical procedure, 50 mL aqueous solution of methylene blue dyes (10 μ M) and 50 mg of the photocatalyst were placed in a 100 mL Pyrex beaker. The mixture was then stirred in the darkness until it reached the adsorption equilibrium. A dark adsorption test was also conducted to compare the adsorption capability of pure TiO₂ and GO-TiO₂ composite. In this test, 50 mg of the photocatalyst was dispersed in 50 mL methylene blue solution (10 μ M). The solution was continuously stirred and kept in the dark for 30 min. Every 15 min, the sample was taken and centrifuged for the UV-visible absorption measurement. From the difference in the absorbance before and after adsorption, the number of dyes adsorbed by the photocatalyst can be estimated.

The photocatalytic reaction was started by turning on the lamp. A 500 W long arc xenon lamp with a UVIRCUT420 optical filter was used as the light source for visible light photocatalytic reaction. After turning on the lamp, the mixture was irradiated for a certain period and stirred incessantly during irradiation. The dye solution was taken from the reactor at regular time intervals and centrifuged to separate the catalyst particles before analysis. The photo-reacted solution was analysed by recording variations of the absorption band maximum (660 nm) in the ultraviolet–visible spectra of methylene blue using an ultraviolet–visible (UV-vis) spectrophotometer (Cary 5000, Agilent, Santa Clara, CA, USA). Direct photolysis in the absence of a photocatalyst was also performed as a blank experiment in order to calculate the contribution from direct photolysis.

4.6. Photocatalytic Disinfection of *E. coli* under Visible Light

The photocatalytic activity of the TiO₂-based material was evaluated by disinfection of *E. coli* under visible light irradiation at room temperature (\approx 23–25 $^{\circ}$ C). Briefly, the *E. coli* K-12 was obtained from the bacterial library in the environment laboratory of Nanyang Technological University. Unless specifically noted, *E. coli* mixing with 50% glycerol (mix

ratio volume/volume = 1/1) was kept in $-80\text{ }^{\circ}\text{C}$ for long-term storage. The experiment was conducted to evaluate the effectiveness of GO-TiO₂ application in cement-based construction materials for the disinfection of *E. coli*. The experimental procedure for the surface study on antibacterial concrete is presented in Figure 12. After 24 h UV/vis light irradiation, 1 mL of *E. coli* suspension was then applied evenly on the cement surfaces using an adjustable precision pipette. The bacteria survival was estimated on an agar dish after 24 h incubation.

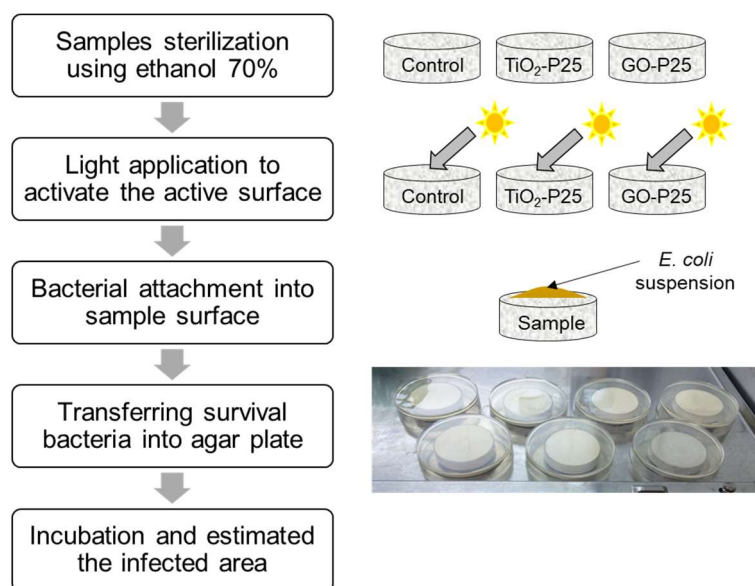


Figure 12. Experimental procedure for the surface study on antibacterial concrete.

5. Conclusions

In this study, visible light-activated graphene-based TiO₂ nanoparticle composites were synthesized through a one-step hydrothermal method. It is found that the combination of GO and TiO₂ in the GO-TiO₂ composite significantly increased the capability of adsorbing the methylene blue dyes compared to the pure TiO₂ materials. More than 60% of the initial dye could be adsorbed into the surface of GO-P25 composites. On the other hand, only 10% of the initial dye was adsorbed by pristine TiO₂. Furthermore, their photocatalytic activity was greatly improved (94% of dye was degraded by GO-P25) in the degradation of methylene blue under visible light irradiation. Conversely, only 36% of the initial dye was degraded by P25 even with longer irradiation time. For antibacterial effect, GO modified TiO₂ sample shows high antibacterial activity compared to pristine TiO₂. The antibacterial effect of the cement-based surface containing 5% of GO-P25 composites shows a 77% reduction of bacteria number. This study confirms the effectiveness of the composites in disinfecting *E. coli* under visible light. This finding is of considerable importance because it may have good potential in the application for future healthcare construction to prevent Hospital-acquired Infection (HAI) cases.

Author Contributions: Conceptualization, A.H.H. and S.Q.; Methodology, A.H.H. and Y.D.; Validation, A.H.H. and Y.D.; Formal Analysis, A.H.H.; Investigation, A.H.H. and Y.D.; Resources, A.H.H., Y.D. and S.Q.; Data Curation, A.H.H. and Y.D.; Writing—Original Draft Preparation, A.H.H.; Writing—Review and Editing, Y.D. and S.Q.; Visualization, A.H.H.; Supervision, S.Q.; Project Administration, A.H.H. and S.Q.; Funding Acquisition, S.Q. All authors have read and agreed to the published version of the manuscript.

Funding: This study was funded by the Academic Research Fund (AcRF) Tier 1 from the Ministry of Education, Singapore (Grant No. RG87/15).

Data Availability Statement: Data is available upon request.

Acknowledgments: This work is part of the author's doctoral thesis—Hamdany, A.H., *Photocatalytic cementitious material for self-cleaning and anti-microbial application*. 2019.

Conflicts of Interest: The authors declare no conflict of interest. The funders had no role in the design of the study; in the collection, analyses, or interpretation of data; in the writing of the manuscript; or in the decision to publish the results.

References

1. Fujishima, A.; Honda, K. Electrochemical Photolysis of Water at a Semiconductor Electrode. *Nature* **1972**, *238*, 37–38. [[CrossRef](#)] [[PubMed](#)]
2. Carp, O.; Huisman, C.L.; Reller, A. Photoinduced reactivity of titanium dioxide. *Prog. Solid State Chem.* **2004**, *32*, 33–177. [[CrossRef](#)]
3. Mills, A.; Le Hunte, S. An overview of semiconductor photocatalysis. *J. Photochem. Photobiol. A Chem.* **1997**, *108*, 1–35. [[CrossRef](#)]
4. Evans, R.C.; Douglas, P.; Burrow, H.D. *Applied Photochemistry [Electronic Resource]*; Evans, R.C., Douglas, P., Burrow, H.D., Eds.; Springer: Dordrecht, The Netherlands, 2013.
5. Fujishima, A.; Zhang, X.T.; Tryk, D.A. TiO₂ photocatalysis and related surface phenomena. *Surf. Sci. Rep.* **2008**, *63*, 515–582. [[CrossRef](#)]
6. Ohama, Y.; Van Gemert, D. *Applications of Titanium Dioxide Photocatalysis to Construction Materials. [Electronic Resource]: State-of-the-Art Report of the RILEM Technical Committee 194-TDP*; Springer Science+Business Media B.V.: Dordrecht, The Netherlands, 2011.
7. Agrios, A.; Pichat, P. State of the art and perspectives on materials and applications of photocatalysis over TiO₂. *Appl. Electrochem.* **2005**, *35*, 655–663. [[CrossRef](#)]
8. Linsebigler, A.L.; Lu, G.; Yates, J.T., Jr. Photocatalysis on TiO₂ surfaces: Principles, mechanisms, and selected results. *Chem. Rev.* **1995**, *95*, 735. [[CrossRef](#)]
9. Endo, M.; Wei, Z.; Wang, K.; Karabiyik, B.; Yoshiiri, K.; Rokicka, P.; Ohtani, B.; Markowska-Szczupak, A.; Kowalska, E. Noble metal-modified titania with visible-light activity for the decomposition of microorganisms. *Beilstein J. Nanotechnol.* **2018**, *9*, 829–841. [[CrossRef](#)]
10. Xiaobo, C.; Mao, S.S. Titanium dioxide nanomaterials: Synthesis, properties, modifications, and applications. *Chem. Rev.* **2007**, *107*, 2891.
11. Braslavsky, S.E. Glossary of terms used in photochemistry, 3rd edition (IUPAC Recommendations 2006). *Pure Appl. Chem.* **2007**, *79*, 293–465. [[CrossRef](#)]
12. Cabir, B.; Yurderi, M.; Caner, N.; Agirtas, M.S.; Zahmakiran, M.; Kaya, M. Methylene blue photocatalytic degradation under visible light irradiation on copper phthalocyanine-sensitized TiO₂ nanopowders. *Mater. Sci. Eng. B* **2017**, *224*, 9–17. [[CrossRef](#)]
13. Vallejo, W.; Diaz-Urbe, C.; Cantillo, Á. Methylene blue photocatalytic degradation under visible irradiation on TiO₂ thin films sensitized with Cu and Zn tetracarboxy-phthalocyanines. *J. Photochem. Photobiol. A Chem.* **2015**, *299*, 80–86. [[CrossRef](#)]
14. Vinodgopal, K.; Hua, X.; Dahlgren, R.L.; Lappin, A.G.; Patterson, L.K.; Kamat, P.V. Photochemistry of Ru(bpy)₂(dcbpy)²⁺ on Al₂O₃ and TiO₂ surfaces. An insight into the mechanism of photosensitization. *J. Phys. Chem.* **1995**, *10883*. [[CrossRef](#)]
15. Chen, C.; Cai, W.; Long, M.; Zhou, B.; Wu, Y.; Wu, D.; Feng, Y. Synthesis of Visible-Light Responsive Graphene Oxide/TiO₂ Composites with p/n Heterojunction. *ACS Nano* **2010**, *4*, 6425–6432. [[CrossRef](#)] [[PubMed](#)]
16. Chen, C.; Long, M.; Zeng, H.; Cai, W.; Zhou, B.; Zhang, J.; Wu, Y.; Ding, D.; Wu, D. Preparation, characterization and visible-light activity of carbon modified TiO₂ with two kinds of carbonaceous species. *J. Mol. Catal. A Chem.* **2009**, *314*, 35–41. [[CrossRef](#)]
17. Du, A.; Ng, Y.H.; Bell, N.J.; Zhu, Z.; Amal, R.; Smith, S.C. Hybrid Graphene/Titania Nanocomposite: Interface Charge Transfer, Hole Doping, and Sensitization for Visible Light Response. *J. Phys. Chem. Lett.* **2011**, *2*, 894–899. [[CrossRef](#)] [[PubMed](#)]
18. Lettmann, C.; Hildenbrand, K.; Kisch, H.; Macyk, W.; Maier, W.F. Visible light photodegradation of 4-chlorophenol with a coke-containing titanium dioxide photocatalyst. *Appl. Catal. B Environ.* **2001**, *32*, 215–227. [[CrossRef](#)]
19. Morales-Torres, S.; Pastrana-Martínez, L.M.; Figueiredo, J.L.; Faria, J.L.; Silva, A.M.T. Design of graphene-based TiO₂ photocatalysts—A review. *Environ. Sci. Pollut. Res. Int.* **2012**, *19*, 3676–3687. [[CrossRef](#)]
20. Nguyen-Phan, T.-D.; Pham, V.H.; Shin, E.W.; Pham, H.-D.; Kim, S.; Chung, J.S.; Kim, E.J.; Hur, S.H. The role of graphene oxide content on the adsorption-enhanced photocatalysis of titanium dioxide/graphene oxide composites. *Chem. Eng. J.* **2011**, *170*, 226–232. [[CrossRef](#)]
21. Zhang, H.; Lv, X.; Li, Y.; Wang, Y.; Li, J. P25-graphene composite as a high performance photocatalyst. *ACS Nano* **2010**, *4*, 380–386. [[CrossRef](#)]
22. Cruz-Ortiz, B.R.; Hamilton, J.W.J.; Pablos, C.; Díaz-Jiménez, L.; Cortés-Hernández, D.A.; Sharma, P.K.; Castro-Alfárez, M.; Fernández-Ibañez, P.; Dunlop, P.S.M.; Byrne, J.A. Mechanism of photocatalytic disinfection using titania-graphene composites under UV and visible irradiation. *Chem. Eng. J.* **2017**, *316*, 179–186. [[CrossRef](#)]
23. Sakka, S. Chapter 11.1.2—Sol–Gel Process and Applications. In *Handbook of Advanced Ceramics*, 2nd ed.; Somiya, S., Ed.; Academic Press: Oxford, UK, 2013; pp. 883–910. [[CrossRef](#)]
24. Mackenzie, J.D. Applications of the sol-gel process. *J. Non-Cryst. Solids* **1988**, *100*, 162–168. [[CrossRef](#)]
25. Suchanek, W.L.; Riman, R.E. Hydrothermal Synthesis of Advanced Ceramic Powders. *Adv. Sci. Technol.* **2006**, *45*, 184–193.
26. Hamdany, A.H. *Photocatalytic Cementitious Material for Self-Cleaning and Anti-Microbial Application*; Nanyang Technological University: Singapore, 2019. [[CrossRef](#)]
27. Simonsen, M.E. Chapter 4—Heterogeneous Photocatalysis. In *Chemistry of Advanced Environmental Purification Processes of Water*; Søgaard, E.G., Ed.; Elsevier: Amsterdam, The Netherlands, 2014; pp. 135–170. [[CrossRef](#)]

28. Cassar, L. Photocatalysis of Cementitious Materials: Clean Buildings and Clean Air. *MRS Bull.* **2004**, *29*, 328–331. [[CrossRef](#)]
29. Hamidi, F.; Aslani, F. TiO₂-based Photocatalytic Cementitious Composites: Materials, Properties, Influential Parameters, and Assessment Techniques. *Nanomaterials* **2019**, *9*, 1444. [[CrossRef](#)]
30. Bawono, A.A.; Tan, Z.H.; Hamdany, A.H.; NguyenDinh, N.; Qian, S.; Lechner, B.; Yang, E.-H. Bright and slip-proof engineered cementitious composites with visible light activated photo-catalysis property for pavement in tunnels. *Cem. Concr. Compos.* **2020**, *114*, 103788. [[CrossRef](#)]
31. Chen, J.; Poon, C.S. Photocatalytic construction and building materials: From fundamentals to applications. *Build. Environ.* **2009**, *44*, 1899–1906. [[CrossRef](#)]
32. Hamdany, A.H.; Ding, Y.; Qian, S. Mechanical and Antibacterial Behavior of Photocatalytic Lightweight Engineered Cementitious Composites. *J. Mater. Civ. Eng.* **2021**, *33*, 04021262. [[CrossRef](#)]
33. Hamdany, A.H.; Ding, Y.; Qian, S. Visible light antibacterial potential of graphene-TiO₂ cementitious composites for self-sterilization surface. *J. Sustain. Cem. Based Mater.* **2022**, *12*, 972–982. [[CrossRef](#)]
34. Hamdany, A.H.; Ding, Y.; Qian, S. Cementitious Composite Materials for Self-Sterilization Surfaces. *ACI Mater. J.* **2022**, *119*, 197–210. [[CrossRef](#)]
35. Hamdany, A.H.; Satyanaga, A.; Zhang, D.; Kim, Y.; Kim, J.R. Photocatalytic Cementitious Material for Eco-Efficient Construction: A Systematic Literature Review. *Appl. Sci.* **2022**, *12*, 8741. [[CrossRef](#)]
36. Krishnan, P.; Zhang, M.-H.; Yu, L.; Feng, H. Photocatalytic degradation of particulate pollutants and self-cleaning performance of TiO₂-containing silicate coating and mortar. *Constr. Build. Mater.* **2013**, *44*, 309–316. [[CrossRef](#)]
37. Poon, C.S.; Cheung, E. NO removal efficiency of photocatalytic paving blocks prepared with recycled materials. *Constr. Build. Mater.* **2007**, *21*, 1746–1753. [[CrossRef](#)]
38. Akhter, P.; Hussain, M.; Saracco, G.; Russo, N. Novel nanostructured-TiO₂ materials for the photocatalytic reduction of CO₂ greenhouse gas to hydrocarbons and syngas. *Fuel* **2015**, *149*, 55–65. [[CrossRef](#)]
39. Banerjee, S.; Dionysiou, D.D.; Pillai, S.C. Self-cleaning applications of TiO₂ by photo-induced hydrophilicity and photocatalysis. *Appl. Catal. B Environ.* **2015**, *176–177*, 396–428. [[CrossRef](#)]
40. Jo, W.-K.; Kang, H.-J. Titanium dioxide–graphene oxide composites with different ratios supported by Pyrex tube for photocatalysis of toxic aromatic vapors. *Powder Technol.* **2013**, *250*, 115–121. [[CrossRef](#)]
41. Liu, J.; Zhu, W.; Yu, S.; Yan, X. Three dimensional carbogenic dots/TiO₂ nanoheterojunctions with enhanced visible light-driven photocatalytic activity. *Carbon* **2014**, *79*, 369–379. [[CrossRef](#)]
42. Pastrana-Martínez, L.M.; Morales-Torres, S.; Likodimos, V.; Figueiredo, J.L.; Faria, J.L.; Falaras, P.; Silva, A.M.T. Advanced nanostructured photocatalysts based on reduced graphene oxide–TiO₂ composites for degradation of diphenhydramine pharmaceutical and methyl orange dye. *Appl. Catal. B Environ.* **2012**, *123–124*, 241–256. [[CrossRef](#)]
43. Zhang, Y.; Pan, C. TiO₂/graphene composite from thermal reaction of graphene oxide and its photocatalytic activity in visible light. *J. Mater. Sci.* **2011**, *46*, 2622–2626. [[CrossRef](#)]
44. Joost, U.; Juganson, K.; Visnapuu, M.; Mortimer, M.; Kahru, A.; Nommiste, E.; Joost, U.; Kisand, V.; Ivask, A. Photocatalytic antibacterial activity of nano-TiO₂ (anatase)-based thin films: Effects on Escherichia coli cells and fatty acids. *J. Photochem. Photobiol. B Biol.* **2015**, *142*, 178–185. [[CrossRef](#)]
45. Zimbone, M.; Buccheri, M.A.; Cacciato, G.; Sanz, R.; Rappazzo, G.; Boninelli, S.; Reitano, R.; Romano, L.; Privitera, V.; Grimaldi, M.G. Photocatalytic and antibacterial activity of TiO₂ nanoparticles obtained by laser ablation in water. *Appl. Catal. B Environ.* **2015**, *165*, 487–494. [[CrossRef](#)]
46. Ebeling, J.; Reinecke, A.; Sibum, N.; Fünfhaus, A.; Aumeier, P.; Otten, C.; Genersch, E. A Comparison of Different Matrices for the Laboratory Diagnosis of the Epizootic American Foulbrood of Honey Bees. *Vet. Sci.* **2023**, *10*, 103. [[CrossRef](#)]
47. Jan, R.; Khan, M.A.; Asaf, S.; Lubna; Lee, I.-J.; Kim, K.M. Metal Resistant Endophytic Bacteria Reduces Cadmium, Nickel Toxicity, and Enhances Expression of Metal Stress Related Genes with Improved Growth of Oryza Sativa, via Regulating Its Antioxidant Machinery and Endogenous Hormones. *Plants* **2019**, *8*, 363. [[CrossRef](#)] [[PubMed](#)]
48. Moon, J.-H.; Won, S.-J.; Maung, C.E.H.; Choi, J.-H.; Choi, S.-I.; Ajuna, H.B.; Ahn, Y.S. *Bacillus velezensis* CE 100 Inhibits Root Rot Diseases (*Phytophthora* spp.) and Promotes Growth of Japanese Cypress (*Chamaecyparis obtusa* Endlicher) Seedlings. *Microorganisms* **2021**, *9*, 821. [[CrossRef](#)] [[PubMed](#)]
49. Imlay, J.A. Pathways of Oxidative Damage. *Annu. Rev. Microbiol.* **2003**, *57*, 395–418. [[CrossRef](#)] [[PubMed](#)]
50. Daly, M.J.; Gaidamakova, E.K.; Matrosova, V.Y.; Vasilenko, A.; Zhai, M.; Leapman, R.D.; Lai, B.; Ravel, B.; Li, S.-M.W.; Kemner, K.M.; et al. Protein Oxidation Implicated as the Primary Determinant of Bacterial Radioresistance. *PLoS Biol.* **2007**, *5*, e92. [[CrossRef](#)]
51. Leung, M.; Chan, A.H.S. Control and management of hospital indoor air quality. *Med. Sci. Monit.* **2006**, *12*, Sr17–Sr23.

Disclaimer/Publisher’s Note: The statements, opinions and data contained in all publications are solely those of the individual author(s) and contributor(s) and not of MDPI and/or the editor(s). MDPI and/or the editor(s) disclaim responsibility for any injury to people or property resulting from any ideas, methods, instructions or products referred to in the content.